Environmental Science & Technology

pubs.acs.org/est

Article

Rapid Emission–Economy Decoupling alongside the Urbanization of Chinese Counties

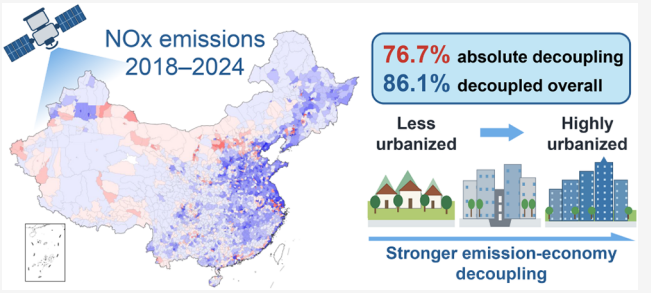
Hao Kong, Jintai Lin,* Sijie Wang, Ruijing Ni, Yuhang Zhang, Mengying Wang, and Chenghao Xu

Cite This: https://doi.org/10.1021/acs.est.6c11406

Read Online

ACCESS | Metrics & More | Article Recommendations | Supporting Information

ABSTRACT: As China makes progress in air pollution control, the growing need for targeted pollution mitigation poses a great challenge for fine-scale emission tracking. However, the lack of up-to-date high-resolution emission data precludes a timely, spatially detailed assessment of emission distributions and their evolution with economic development. Here we derive summertime nitrogen oxides emissions from 2018 to 2024 for a total of 2,842 counties at different levels of urbanization in mainland China, based on satellite measurements and a fast, physics-based emission inversion method. The results show widespread declines in 84.1 ± 7.3% of counties. Among the 1,779 counties with available gross domestic product data, 76.7 ± 7.1% achieve absolute emission-economy decoupling (i.e., reduced emissions despite economic growth), and an additional 9.4 ± 3.9% exhibit relative decoupling (i.e., economic growth outpacing emissions growth). Relative emission reductions and emission-economy decoupling tend to be stronger in more urbanized counties, with the share of total national emissions moving toward less-urbanized, previously less-focused counties, particularly in the west. These results suggest structural progress toward greener development in Chinese counties along with an emerging need to shift attention toward less-urbanized locations.



KEYWORDS: *Environmental regulation, Emission-economy decoupling, County-level analysis, Satellite remote sensing, Nitrogen oxides emission inversion*

1. INTRODUCTION

China has made effective progress in air quality management, as a result of its ambitious and coordinated three-phased national strategies,[1−3] which emphasize stage-based reduction targets, key sectors and regions, and a shift toward finer-scale emission source control with nationwide implementation. Yet further air quality improvement will have to navigate location-specific challenges to achieve targeted emission control. In the ongoing third-phase national policy,[3] counties have become key administrative units in the monitoring of air quality and emissions aiming for accurate source identification and effective mitigation measures. Meanwhile, the policy further emphasizes balancing economic growth with environmental regulation.[3] Thus, timely high-resolution emission information that tracks county-level pollution is vital for assessing emission-reduction effectiveness and systematically evaluating emission-economy decoupling. However, accurate and up-to-date data of county-level emissions and trends in recent years are still lacking, mainly due to the limitations of conventional emission inventories and ground-based monitoring.

Information to characterize county-level emissions is often lacking in developing countries such as China, posing a major constraint on the spatial resolution of current bottom-up inventories.[4,5] A typical bottom-up approach relies on proxy-based (such as nighttime light and population density)[4] downscaling to allocate national or provincial emissions to target grids at 10 km resolution or coarser. Although specific geolocation information is available for certain point sources, this information often does not keep pace with the temporal dynamics of point sources,[6] such as the retirement and new establishment of power plants.[7] Thus, the bottom-up approach alone is unable to account for locally distinctive socioeconomic and pollution patterns and associated emissions. Although some local inventories adopt more detailed activity data (e.g., industrial production and fuel consumption at city or county level) to assess emissions at finer scales,[8,9] their time lags of 4−5 years or more preclude an up-to-date analysis. Extending such methods to less-developed regions, where the gaps in human activity data remain pervasive, is particularly challenging.

Although air pollution information can be obtained in time from ground-based monitoring, its limited spatial coverage and representativeness remain a major bottleneck.[10] Only about

Received: July 24, 2026
Revised: October 22, 2026
Accepted: October 23, 2026

ACS Publications © XXXX American Chemical Society

Downloaded from pubs.acs.org/esthag/article-pdf/doi/10.1021/acs.est.6c11406/6919082S/acs.est.6c11406.pdf by PEKING UNIV user on 19 November 2026

one-third of counties in China contain air quality sites as part of the national environmental monitoring network overseen by the Ministry of Ecology and Environment (MEE, see the discussion in Section 4). As a result, observation-based emission inversion from this network often relies on a limited number of sites to constrain emissions across multiple counties. This limitation is particularly severe in the western regions[11] where anthropogenic emissions are becoming increasingly important.[10] Moreover, the monitoring sites are concentrated in urban areas but sparse in suburban and rural areas; and such an uneven distribution can bias the inferred emission trends,[12,13] especially in less urbanized counties. Indeed, the regions containing MEE sites tend to achieve greater emission reductions,[13] biasing the observed pollution trends.

Consequently, current understanding of China's emission-economy transition is primarily understood from large-scale analyses. Such spatial aggregation could mask the actual extent of emission-economy decoupling, as our previous analyses across prefectural cities (higher-level administrative units encompassing counties) have already revealed substantial heterogeneity in emission changes[10] that is largely overlooked in previous studies. Moreover, the relationship between emissions and economic development is strongly shaped by urbanization, a key factor that may exert different or even opposite effects across different development stages.[14] However, how urbanization affects emission-economy decoupling across counties at China's current stage of development remains poorly quantified. Clearly, reliable county-level emission estimates are a prerequisite for comprehensively evaluating emission-economy decoupling and its variation across urbanization levels.

Satellite remote sensing provides near-real-time observations of atmospheric composition with near-global coverage at high resolution (e.g., 5 km), enabling finer-scale emission tracking to compensate for the above-mentioned limitations of emission inventories and ground-based measurements. However, satellite-based emission inversions using three-dimensional chemical transport models (CTMs) are too computationally expensive to achieve wide spatial coverage, fine resolution and timely estimation simultaneously.[15,16] To address this challenge, here we adopt PHLET,[17,18] a fast physics-based inversion framework at 0.05° × 0.05° (~5 × 5 km^2) resolution accounting for location-specific horizontal transport and nonlinear chemistry, to estimate county-level summertime emissions of nitrogen oxides (NO_X = NO + NO_2) from 2018 to 2024 in mainland China. NO_X is a short-lived criteria air pollutant strongly tied to urbanization and industrial development, a main precursor of ozone and fine particulate matter ($PM_{2.5}$) pollution, and an increasingly important target of emission regulation across China's three-phased air-quality management strategies.[3] High-quality satellite measurements of NO_X, together with its short lifetime and reliable emission inversion methods, allow pinpointing anthropogenic sources[19] and assessing coemitted species including carbon dioxide (CO_2).[20] Based on the 5-km PHLET inversion, our study establishes a high-quality county-level NO_X emission data set for mainland China during 2018−2024, and further integrates it with economic and urbanization indicators to systematically assess fine-scale emission changes across counties and emission-economy transition across different urbanization levels.

2. MATERIALS AND METHODS

2.1. POMINO-TROPOMI NO_2 VCDs

For NO_X emission inversion, tropospheric NO_2 VCD data in summer (June, July and August) from 2018 to 2024 are obtained from the POMINO-TROPOMI v1.2.2 product. The TROPOMI sensor is on board the sun-synchronous Copernicus Sentinel-5 Precursor satellite launched in October 2017. It provides remote sensing of NO_2 at the overpass time around 13:30 (local solar time) with daily global coverage since May 2018. With a swath of 2600 km, it was initially operated with a nadir pixel size of about 3.5 km × 7 km, which was reduced to about 3.5 km × 5.5 km since August 2019.[21] We use summertime emissions to demonstrate the interannual variabilities; the seasonal variability of NO_X emissions is relatively stable from one year to another (within 1.5%), according to the emission inventories[10] (Figure S1).

The POMINO algorithm for tropospheric NO_2 VCDs was established in 2014 and has been applied to the OMI, TROPOMI and GEMS sensors with various updates.[22−26] Compared to the respective official products, POMINO-TROPOMI shows higher consistency with ground-based measurements with smaller biases.[25] And it contains more valid observations especially in polluted situations with heavy aerosol and NO_2 loadings, and thus reduces the systematic sampling biases in average NO_2 VCDs and the derived emissions.[22,25] POMINO explicitly accounts for the effects of aerosols and surface reflectance anisotropy and uses a priori NO_2 vertical profiles at a finer horizontal resolution (25 km versus 100 km in the official TROPOMI algorithm) to calculate air mass factors (AMFs). These AMFs are then applied to convert tropospheric NO_2 slant columns, obtained from the official retrieval, to vertical columns.[25]

In POMINO-TROPOMI version 1.2.2, updated auxiliary data sets are incorporated, and the a priori NO_2 and aerosol profiles are interpolated to a 5-km grid to prevent artificial discontinuities along grid boundaries in NO_X emission inversion.[17] The NO_2 VCDs in this version significantly reduce the systematic underestimation relative to ground-based measurements reported in the former versions.[17,27,28] Therefore, the scaling adjustment on NO_2 VCDs applied to previous versions to correct for systematic biases[17] is not employed in this study.

To obtain valid data, Level-2 tropospheric NO_2 VCD pixels are filtered out with 1) qa_values (adopted from the official product) ≤ 0.5 to avoid problematic retrievals; 2) POMINO-calculated cloud radiance fraction >0.5 to remove cloud-covered scenes (which, in combination with criterion 1, is equivalent to qa_values ≤ 0.75 in the official TROPOMI product); 3) aerosol optical depth (AOD) > 3 to avoid invalid retrieval affected by heavy aerosol loading; 4) solar zenith angle (SZA) or viewing zenith angle (VZA) > 80°; and 5) surface albedo (derived from bidirectional reflectance distribution function, BRDF) > 0.3.[17,28]

The selected Level-2 pixels are then resampled to a 0.05° × 0.05° grid (i.e., Level-3 data for emission inversion) through an oversampling approach.[18] Since the satellite pixels do not align (in size, shape and orientation) with the PHLET model grid used for emission inversion, a satellite conversion matrix (SCM)[18] is generated alongside the oversampling to account for the effects of varying pixel shape, size and orientation. The SCM projects PHLET-modeled NO_2 on the 0.05° × 0.05° grid to each TROPOMI pixel, and then back to the model grid, enabling appropriate, effective comparison between model simulations and satellite observations.[18]

To better isolate near-surface NO_2 associated with sources on the ground and distinguish emission hotspots, a location-dependent background is subtracted from the tropospheric NO_2 VCDs. The background value is estimated by calculating the 1% quantile values of the level-3 NO_2 VCDs within a moving window of 500 km,[17] and subsequently applying a 500-km moving average to remove potential outliers.

2.2. NO_X Emission Inversion by PHLET

The PHLET model, together with its adjoint model, simulates the nonlinear lifetime-abundance response and horizontal transport at

Downloaded from pubs.acs.org/esthag/article-pdf/doi/10.1021/acs.est.6c11406/6919082S/acs.est.6c11406.pdf by PEKING UNIV user on 19 November 2026

https://doi.org/10.1021/acs.est.6c11406
Environ. Sci. Technol. XXXX, XXX, XXX−XXX

each grid cell to allow fast inversion of NO_X emissions from NO_2 VCDs.[17,18] PHLET enables high-resolution (i.e., 5 km or finer) emission inversion for a large domain (e.g., mainland China in this study) with high accuracy. The model assumes a steady state of debackgrounded NO_2 VCDs in the early afternoon, when averaged over multiple days (in summer here), and accounts for the horizontal transport and nonlinear chemistry of NO_2. This differs from traditional inversion methods based on 3-dimensional chemistry transport models (CTMs) with adjoint or Kalman filter, which require expensive computational resources.

Here we follow the processes for NO_X emission inversion in ref.[17] Wind fields (around 0−500 m above the ground) from the GEOS-FP assimilated meteorological data are used to calculate the horizontal transport in PHLET.[17] To calculate the NO_2-to-NO_X ratio at each grid cell, a multivariate regression built based on GEOS-Chem simulations is adopted.[17] This regression uses the regional mean NO_2 concentration, local NO_2 enhancement relative to the regional mean, wind speed, temperature, and leaf area index as predictors, and reproduces the GEOS-Chem simulated NO_2-to-NO_X ratio with a normalized RMSE of 5% and a correlation coefficient of 0.97.[17] To account for the effective NO_2 lifetime, the local net source (emissions minus total loss, including chemistry and deposition) of NO_X is first inferred.[17,18] Then the nonlinear relationship between NO_2 VCD and NO_X loss for lifetime estimation, with four parameters, is fitted over low-emission areas within each 5° × 5° region, where emissions are assumed to be negligible; and the fitted relationship is subsequently applied to the entire subregion to derive the lifetime at each grid cell.[17,18] Overall, the effective NO_2 lifetime over mainland China decreased by 3.6% from 2018 to 2024, consistent with recent enhancement of atmospheric oxidation capacity.[29,30] Different low-emission area selection criteria are considered to account for uncertainties associated with the effective NO_2 lifetime following ref. 17.

To assess the overall inversion uncertainties at different spatial scales (e.g., national and county levels), including uncertainties in temporal trends and the fractions of counties in different classification categories (e.g., different extents of emission-economy decoupling), a 50-member Monte Carlo test is conducted. Following uncertainty considerations in ref,[17] the test accounts for uncertainties from satellite NO_2 VCD, background removal, steady-state assumption, meteorological data, NO_2 lifetime, NO_2-to-NO_X ratio, and other procedures. All uncertainties reported represent 1-σ uncertainties, unless otherwise specified.

The emissions derived above include the contributions of both anthropogenic and natural (open fires and soil) surface sources. To extract the anthropogenic contributions, we adopt NO_X emissions from soil (based on ref. 31) and fires (GFAS v1.2, last access: March 3, 2025)[32] from the public data sets, and subtract them from the satellite-derived emissions. Since the soil NO_X emission data set is not available for 2024, we follow ref. 10 to conduct the emission calculation for 2024 by using HEMCO v3.10.1 (embedded in GEOS-Chem v14.5.1[33]) and GEOS-FP meteorological data (last access: February 14, 2025). The interannual variations of soil and fire emissions are shown in Figure S2a−b. The subtracted soil and fire emissions together are about 7.3% of PHLET-derived total emission (based on results in summer 2018). Besides the above soil and fire NO_X emissions, many less-known natural NO_X sources likely exist in vast remote regions.[10,34] Therefore, we remove all emissions from grid cells with no evidence of human activities indicated in several proxies[17] including Tencent location data,[35] nighttime light,[36] and road network;[37] the removed emissions are about 7.7% of PHLET-derived total emission.

2.3. Validation of Derived Emissions

To evaluate the quality of PHLET-derived emissions, we conduct a comprehensive set of tests, including 1) comparing the performance of near-surface NO_2 concentrations simulated by two CTMs (at different resolutions) driven by PHLET and other emission data sets; 2) comparing the PHLET emissions with in situ surface flux measurements; and 3) examining the consistency between PHLET emissions and an independent emission data set inferred from near-surface NO_2 concentration measurements. Overall, these tests support the reliability of the PHLET-derived emissions, providing a basis for the subsequent county-level analysis.

2.3.1. Improved GEOS-Chem Simulations over Mainland China. To evaluate the quality of our PHLET-derived NO_X emissions, we first adopt the nested GEOS-Chem v14.5.1[33] (70°−140°E, 15°−55°N at 0.3125° longitude × 0.25° latitude with 47 vertical layers) to simulate the near-surface NO_2 concentrations over mainland China in June from 2018 to 2024. The nested GEOS-Chem model is driven by either PHLET-derived anthropogenic NO_X emissions or the widely used MEIC v1.4 (last access: August 4, 2023) emission inventory[4,5] for comparison; MEIC v2.0 is used as a further test. These model simulations are compared with ground-based measurements from the MEE for evaluation.

Meteorological fields to drive the GEOS-Chem simulations are adopted from the GEOS-FP assimilated data. GEOS-Chem is driven with the full O_X-NO_X-VOC−CO-HO_X gaseous chemistry and online aerosol calculations using an autoreduce solver.[38] It adopts the relaxed Arakawa-Schubert scheme for convection,[39] and a nonlocal scheme for vertical mixing in the planetary boundary layer implemented by Lin et al.[40] Dry deposition follows ref[41] with modifications for gases[42] and aerosols.[43] The lateral boundary conditions of the nested model are obtained from global 5° longitude × 4° latitude simulations in corresponding years. A one-week spin-up of the nested modeling is performed to minimize initialization effects.

The MEIC v1.4 is openly available for 2020 and prior years. To drive the simulations for 2021−2024, we scale the MEIC NO_X emissions in 2020 to other years based on the respective ratios in PHLET national total anthropogenic emissions in mainland China. Emissions of the other species are adopted from MEIC, and kept unchanged after 2020. The diurnal cycles of emissions in each sector are adopted from MEIC; and the resulting gridded diurnal cycles for anthropogenic NO_X emissions are applied to the PHLET-driven simulations. All other emissions and model setups are the same in the two sets of simulations.

The simulated NO_2 concentrations in the bottom layer (centered at ∼65 m above the ground) are compared with MEE measurement data. To ensure sampling consistency, GEOS-Chem simulation results where and when there are missing/invalid MEE measurements are removed. Valid hourly MEE measurements are first aggregated to the GEOS-Chem grid (0.3125° × 0.25°). Then, the hourly simulations are filtered according to the gridded hourly MEE data. Finally, the gridded observations and simulations are averaged to daily and monthly means for comparison.

The MEE sites provide hourly measurements, and are filtered by the following standards. 1) If more than 8 records of hourly measurements within a day are either 0 or missing, then all measurements on that day are considered invalid and removed; 2) if more than 10 days of observations are removed/invalid in June of a particular year, then all measurements in all years from the site are screened out.[10] After the filtering, there remain 1,174 sites to be used. Subsequently, the valid hourly measurements from all sites are contamination corrected (see next paragraph), and then averaged within each of the GEOS-Chem grid cells (or within each county for a county-level comparison).

Prior to the spatial and temporal averaging, we correct for potential biases in the hourly MEE measurements due to contamination by other nitrogen species, following eq 1.[44]

$$C_{\mathrm{MEE}}^{\mathrm{NO_2 corrected}} = C_{\mathrm{MEE}}^{\mathrm{NO_2}} \cdot \frac{\mathrm{NO_2}}{\mathrm{NO_2} + \Sigma\mathrm{AN} + 0.95\,\mathrm{PAN} + 0.35\,\mathrm{HNO_3}} \quad (1)$$

where NO_2, ΣAN, PAN and HNO_3 are GEOS-Chem-simulated nitrogen species, separately for the simulations driven by PHLET-derived and MEIC NO_X emissions. This correction is applied to the hourly gridded data for the comparison between GEOS-Chem simulations and MEE observations, but not to the county-level pollution trend analyses shown in Figures S3 and S4, which do not

Downloaded from pubs.acs.org/esthag/article-pdf/doi/10.1021/acs.est.6c11406/6919082S/acs.est.6c11406.pdf by PEKING UNIV user on 19 November 2026

https://doi.org/10.1021/acs.est.6c11406
Environ. Sci. Technol. XXXX, XXX, XXX−XXX

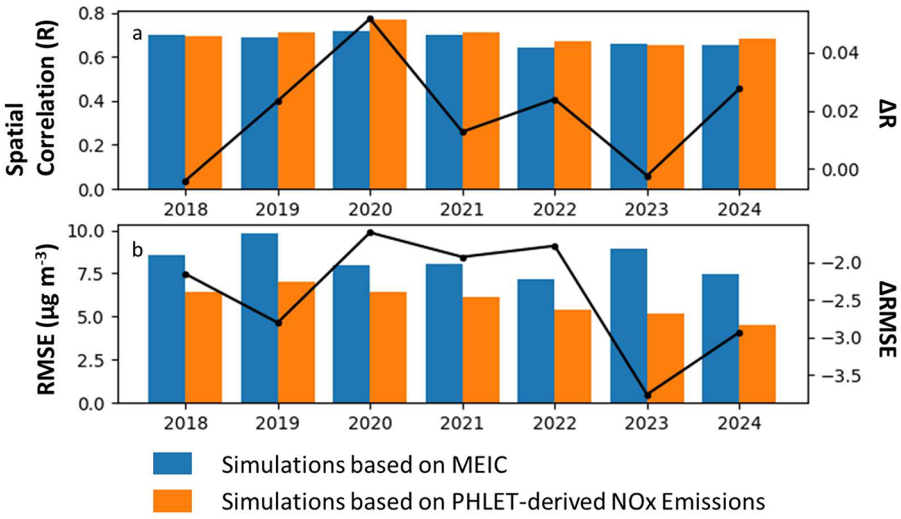


Figure 1. Evaluation of PHLET-derived emissions based on ground measurements. Spatial correlations (a), RMSEs (b) between contamination-corrected MEE measurements (eq 1) and GEOS-Chem simulations, based on MEIC v1.4 and PHLET-derived NO_X emissions, respectively, for monthly daily average NO_2 concentrations in June from 2018 to 2024. The black lines indicate the annual differences between the PHLET- and MEIC-driven simulations.

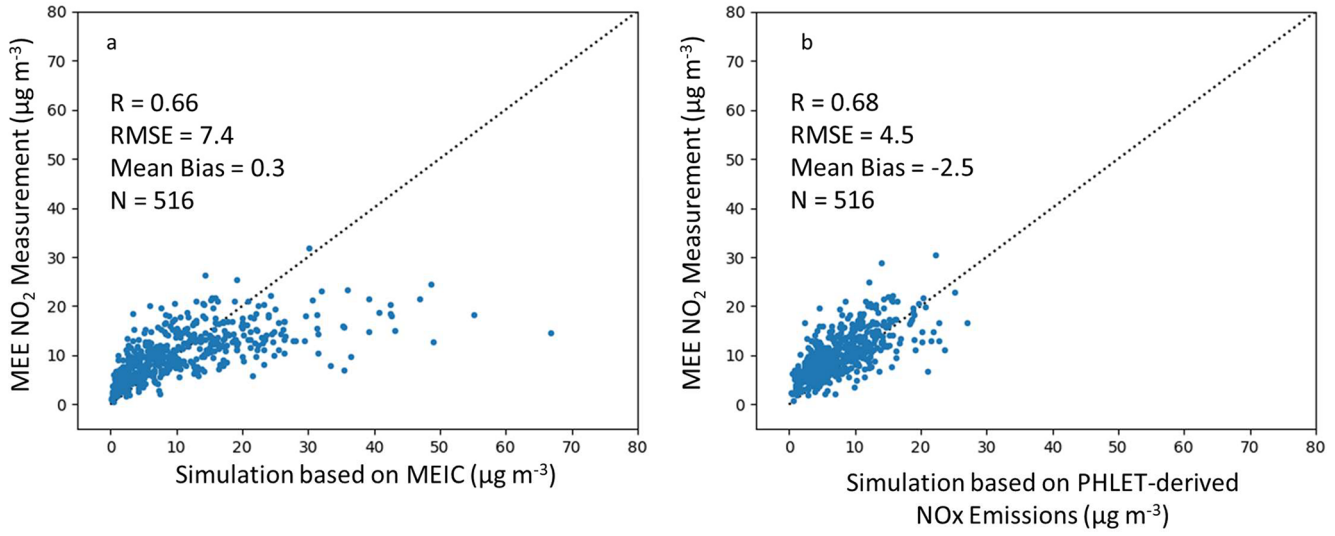


Figure 2. Scatter plots comparing contamination-corrected MEE NO_2 measurements (eq 1) with simulated June 2024 NO_2 concentrations (monthly averages of daily mean values), based on NO_X emissions from MEIC v1.4 (a) and PHLET (b). Linear fitting results are given in Table S1. Here, each data point represents a grid cell at 0.3125° × 0.25°.

involve model-observation comparisons and are not affected by such a correction.

As shown in Figure 1a–b, in June 2018–2024, PHLET-derived NO_X emissions improve the spatial correlations between the simulated monthly averages of daily mean NO_2 concentrations and MEE measurements, and substantially decrease the root-mean-square errors (RMSEs, from 7.2 to 9.9 $\mu g\ m^{-3}$ to 4.5–7.0 $\mu g\ m^{-3}$ across the years), compared with the simulations driven by MEIC v1.4. Figure 2 further shows the scatter plots of MEE measurements and simulated spatial distributions of monthly daily mean NO_2 concentrations in June 2024 based on MEIC and PHLET-derived NO_X emissions. The MEIC-driven simulation shows a much greater range of NO_2 concentrations than MEE measurements, resulting in substantial positive biases in high-value areas and negative biases in low-value areas. By comparison, the PHLET-driven simulation does not exhibit such a bias pattern. A comprehensive set of statistics for model evaluation in all study years is provided in Table S1, including information for R, RMSE, mean bias, and slope and intercept of linear fit; overall, these statistics suggest a general improvement of model simulations when PHLET emissions are used.

Note that in Figure 2, a slight underestimation is observed at the low concentration range (<10 $\mu g\ m^{-3}$) for simulations driven by both emission data sets, which may reflect uncertainties in regional background NO_2 levels (e.g., due to unrepresented natural sources in CTMs[10,34]) and transport processes. In addition, MEE monitoring sites are typically located in populated areas, whereas the model represents grid-cell mean concentrations, potentially leading to higher observed concentrations than simulated values, since each model grid cell may contain both high- and low-NO_2 locations.[45] This effect is related to the spatial representativeness limitation of MEE observations, which is important for short-lived pollutants like NO_X.

We further evaluate whether the PHLET-derived emissions capture observed temporal changes in near-surface NO_2. The spatial distribution of interannual changes between different years in simulated June NO_2 concentrations is compared with those observed by MEE at collocated model grid cells. The PHLET-driven

https://doi.org/10.1021/acs.est.6c11406
Environ. Sci. Technol. XXXX, XXX, XXX−XXX

Downloaded from pubs.acs.org/esthag/article-pdf/doi/10.1021/acs.est.6c11406/6919082S/acs.est.6c11406.pdf by PEKING UNIV user on 19 November 2026

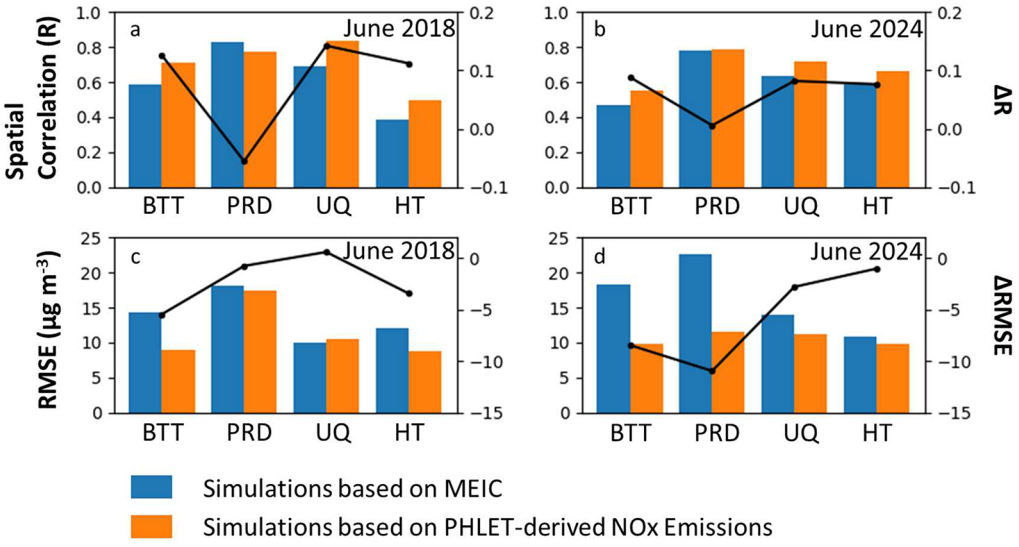


Figure 3. Evaluation of PHLET-derived emissions based on ground measurements. Spatial correlations (a–b), RMSEs (c–d) between contamination-corrected MEE measurements (eq 1) and WRF-Chem simulations, based on MEIC v1.4 and PHLET-derived NO_X emissions, respectively, for monthly daily average NO_2 concentrations in June 2018 and June 2024. The black lines indicate the differences between the PHLET- and MEIC-driven simulations. BTT: Beijing-Tianjin-Tangshan region; PRD: the Pearl River Delta; HT: the Hetao region; UQ: the Urumqi area.

simulations generally reproduce the observed changes better than the inventory-driven simulations (Figure S5a–b).

Additionally, the MEIC inventory has been updated to v2.0 in 2025, with emission data for 2021–2023 becoming available. Thus, we further repeat the simulations for 2021–2023 using MEIC v2.0 instead of using PHLET to scale emissions for these three years. We find that the PHLET-driven simulations show consistent improvements over the simulations driven by MEIC v2.0 (Figure S6), similar to the results comparing PHLET- and MEIC v1.4-driven simulations.

2.3.2. Improved Regional WRF-Chem Simulations at High Resolution. To further evaluate the fine-scale performance of our PHLET-derived NO_X emissions, we conduct 3-km-resolution WRF-Chem v3.9.1[46−48] simulations over four representative emission hotspot clusters across China, including the Beijing-Tianjin-Tangshan region, the Pearl River Delta, the Hetao region, and the Urumqi area (domains shown in Figure S7). Similar to the GEOS-Chem-based validation, the model is driven by PHLET and MEIC v1.4 NO_X emissions to simulate the near-surface NO_2 in June 2018 and June 2024. The simulated NO_2 concentrations in the bottom layer (centered at ∼15 m above the ground) are compared with contamination-corrected MEE ground-based measurements. Similar quality-control filtering is applied to the MEE measurements, except that the site screening is performed independently for each year to retain a sufficient number of valid sites (>10) in each region.

The regional WRF-Chem simulations adopt the National Centers for Environmental Prediction (NCEP) Final Operational Global Analysis (FNL) data set (last access: May 21, 2025) for meteorological initial and boundary conditions, and the nested GEOS-Chem simulations for the chemical initial and boundary conditions. The simulations use the Model for Simulating Aerosol Interactions and Chemistry (MOSAIC-4 bin) and the Carbon Bond Mechanism-Z for aerosol and gas-phase chemistry calculations, respectively.[47,48]

As shown in Figure 3, simulations driven by the PHLET-derived NO_X emissions show better agreement with the MEE observations in most cases, with substantially higher spatial correlations and lower RMSEs. On average, the spatial correlation is improved by 13.0% in June 2018 and 10.2% in June 2024, while the RMSE is reduced by 16.5% and 35.3%, respectively. These high-resolution modeling results further support the added value of PHLET emissions upon the existing emission inventories.

The temporal changes in near-surface NO_2 are also examined using the 3-km WRF-Chem simulations for June 2018 and June 2024 over the four regions. At this finer resolution, the improvement associated with PHLET-derived emissions becomes more evident. For example, over the Beijing-Tianjin-Tangshan region, the spatial correlation between simulated and observed NO_2 changes increases from 0.19 with inventory emissions to 0.57 with PHLET emissions (Figure S5c).

2.3.3. Comparison with in-situ Fluxes and Ground-Measurement-Based Emission Inversion. To provide additional validation using independent data sets, we compare the PHLET-derived NO_X emissions with summertime in situ eddy-covariance flux measurements from a flux tower in Beijing[49,50] (location shown in Figure S7), after accounting for the measurement footprint.[49,50] As shown in Figure S8, the PHLET-derived emissions in 2018 are 31.0% higher than the flux measurements in 2017, likely reflecting interannual variability; and in 2023, the PHLET-derived emissions differ from the corresponding flux by only 14.5%. These differences are smaller than those between the flux measurements and three widely used emission inventories (Figure S8). More importantly, PHLET shows a substantial emission decline (by 52.5% from 2018 to 2023), which is close to the observed decrease (by 45.6% from 2017 to 2023), compared with the much weaker declines in the inventories (by 6.0–30.8% from 2017 to 2023; to 2022 for EDGAR).

We further compare the PHLET-derived emissions with the Inversed Emission Inventory for Chinese Air Quality (CAQIEI, last access: October 31, 2024), which is an independent emission inversion data set derived based on near-surface NO_2 concentration measurements from the MEE monitoring network. PHLET shows substantially higher agreement with CAQIEI than the agreement between CAQIEI and three emission inventories over counties covered by the MEE network (R = 0.57 versus 0.14–0.24; Table S2).

2.4. County-Level Emission and Urbanization Rate

Our analysis is focused on county-level emissions for a total of 2,842 county-level administrative divisions in mainland China. According to China's official administrative designation, these county-level divisions include 977 urban districts, 395 county-level cities and 1,470 counties (including 52 ethnic autonomous counties, aka. "banners" in Inner Mongolia). Urban districts and county-level cities exhibit much higher levels of urbanization than other county-level administrative divisions,[51] based on urbanization rate (UR, officially defined as the proportion of urban population) in 2020. Hereafter, unless stated

https://doi.org/10.1021/acs.est.6c11406
Environ. Sci. Technol. XXXX, XXX, XXX−XXX

Downloaded from pubs.acs.org/esthag/article-pdf/doi/10.1021/acs.est.6c11406/6919082S/acs.est.6c11406.pdf by PEKING UNIV user on 19 November 2026

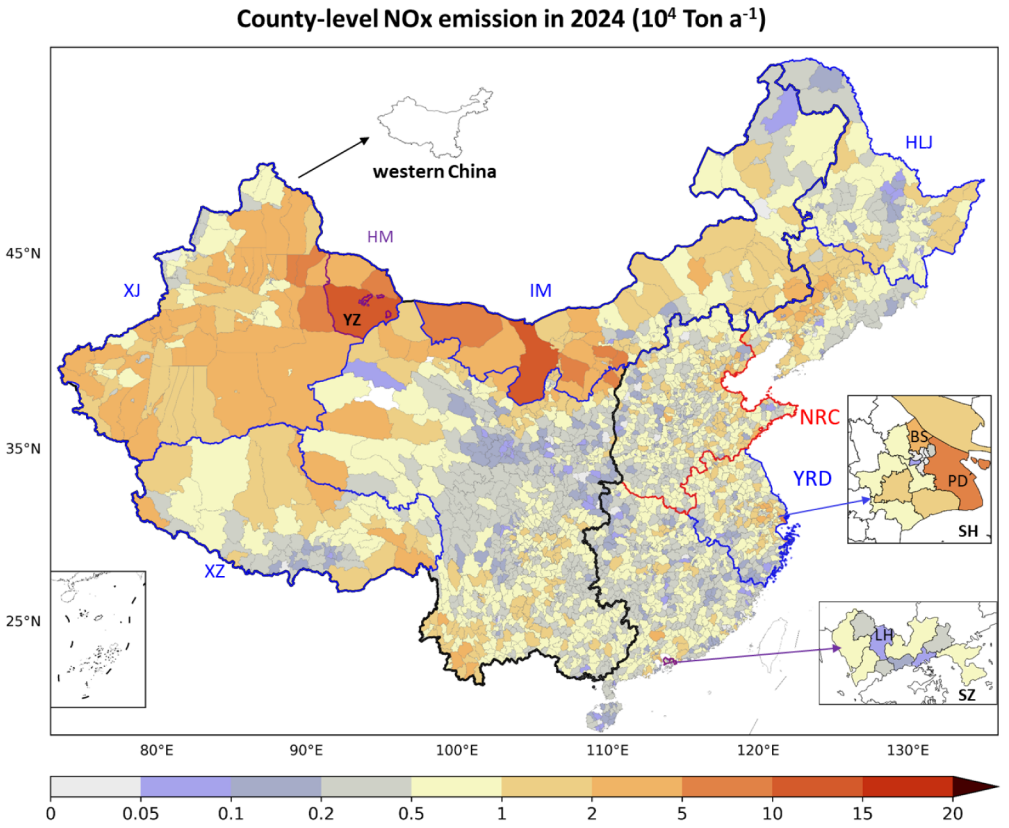


Figure 4. County-level NO_X emissions in summer 2024. The area varies by several orders of magnitude across the counties. The black bold boundary denotes western China. The blue boundaries denote the provinces mentioned in the main text (IM: Inner Mongolia, HLJ: Heilongjiang, XJ: Xinjiang, and XZ: Xizang, aka. Tibet), and the Yangtze River Delta (YRD). The red boundary denotes the North China Region (NRC). The purple boundaries denote cities mentioned in the main text (HM: Hami, and SZ: Shenzhen). And the county-level Yizhou District (YZ) within Hami City is also marked. The insets further illustrate emissions in the districts of Shenzhen and Shanghai (except Chongming Island). Baoshan (BS) District and Pudong New Area (PD) within Shanghai and Longhua (LH) District within Shenzhen are marked in the insets. Administrative boundaries are adopted from ref. 52

otherwise, we simply refer to all county-level administrative divisions as "counties" without distinction. We employ county boundaries from ref. 52 (last access: April 15, 2025) to determine the geographical coverage. To better align the gridded emission data with county boundaries, the original 0.05° × 0.05° emission data are interpolated onto a 0.01° × 0.01° grid. The total emissions for each county are then calculated by summing over the 0.01° × 0.01° grid cells whose centers fall within the county boundaries.

As the county-level UR data are often unavailable in the official statistics, we estimate URs by integrating gridded population density data at a spatial resolution of 100 m from China's Seventh National Population Census (for 2020)[53] with land-use classifications from the GHSL data set at a spatial resolution of 1 km (GHS-SMOD, for 2020).[54] Both data sets are first resampled to the 0.01° × 0.01° grid. The urban and rural populations in each county are then calculated by aggregating population counts over grid cells classified as urban and nonurban, respectively. Finally, the UR is calculated as the ratio of the urban population to the total population from the grid cells within each county. The resulting county-level URs are shown in Figure S9. Here, temporal variations in UR are not considered, because the census-based population data are updated at relatively long intervals (10 years). Moreover, both population distribution and urban land area are supposed to have much weaker temporal dynamics than air pollution and economic indicators.

3. RESULTS

3.1. Substantial NO_X Emission Differences across Counties

Based on PHLET inversion and POMINO-TROPOMI NO_2 VCDs, we first quantify summertime NO_X emissions for 2,842 counties across mainland China to address the current lack of up-to-date knowledge of county-level emission characteristics. Substantial spatial variability is observed across the counties (Figure 4). In summer 2024, the total anthropogenic NO_X emissions from the counties are $1.80 \pm 0.31 \times 10^7$ Ton a^{-1} (or 0.55×10^7 Ton N a^{-1}). Here, the summertime emission is expressed on a per-year basis by using a scaling factor of 365/92, following the conventional notation. This emission amount represents the early afternoon value, given the overpass time of satellite instrument at about 13:30 local solar time (LST); scaling the early afternoon emission to daily mean based on its diurnal cycle[55−57] would result in an approximately 20% lower estimate.

About 65.1% of the national total emissions are contributed by 80% of the counties (from the 10th to 90th percentile ordered by emissions), among which NO_X emissions span approximately 1 order of magnitude from 0.13×10^4 to 1.21×10^4 Ton a^{-1}. Counties in the lowest emission decile are mainly located in eastern China (200 out of 285); together, they contribute only 1.1 ± 0.1% of the national total. These low-emission counties are located in remote areas with limited human activities, such as northern Heilongjiang Province, or in

https://doi.org/10.1021/acs.est.6c11406
Environ. Sci. Technol. XXXX, XXX, XXX−XXX

Downloaded from pubs.acs.org/esthag/article-pdf/doi/10.1021/acs.est.6c11406/6919082S/acs.est.6c11406.pdf by PEKING UNIV user on 19 November 2026

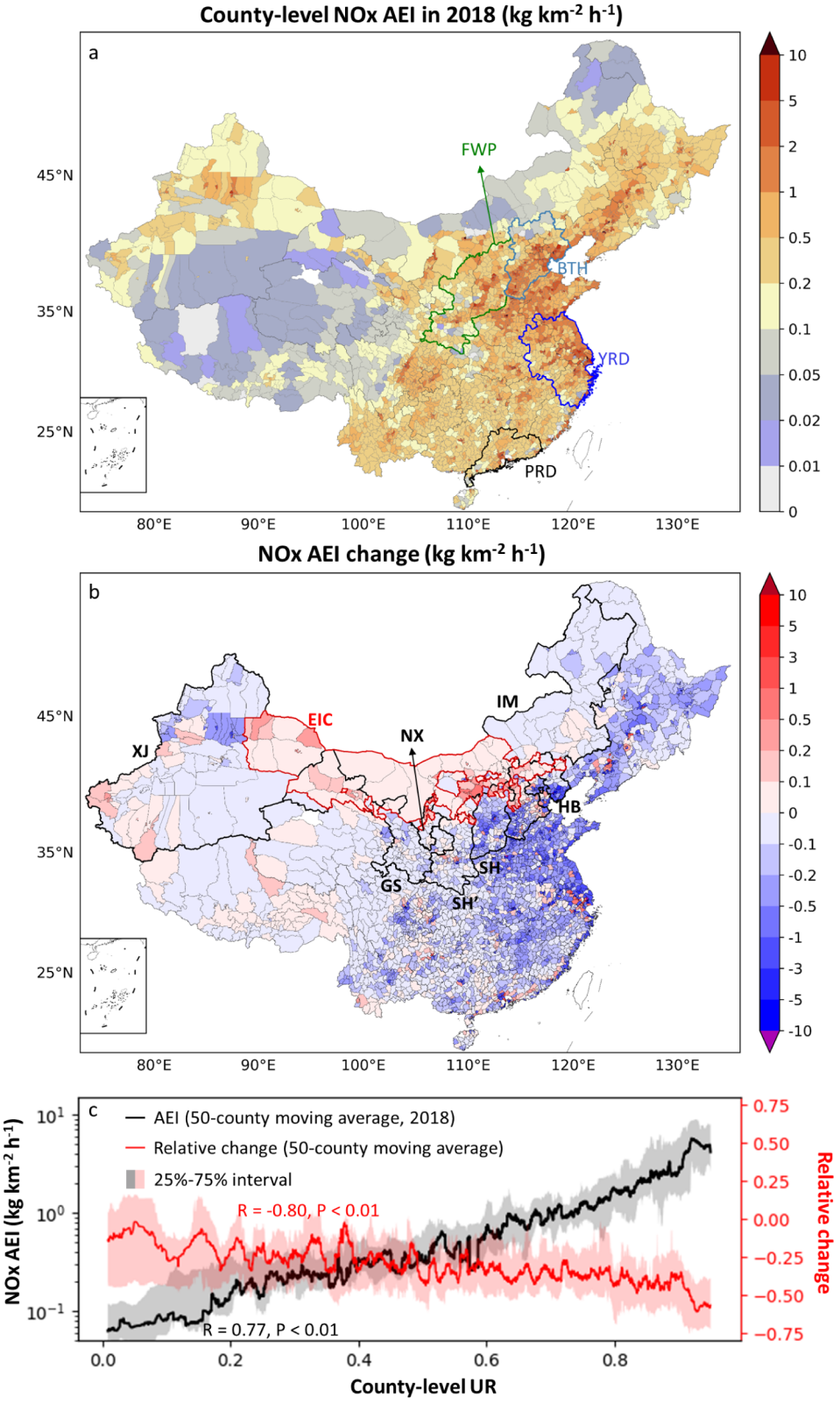


Figure 5. Spatial disparity in county-level emission changes. (a) County-level NO_X AEIs in 2018. The cities and regions mentioned in the main text are marked (FWP: Fenhe-Weihe Plain, BTH: Beijing-Tianjin-Hebei, YRD: Yangtze River Delta, and PRD: Pearl River Delta). (b) Changes in county-level NO_X AEIs from 2018 to 2024. The emission-increasing cluster (EIC) in the west is marked with red boundaries. Several provinces are marked with black bold boundaries (XJ: Xinjiang, NX: Ningxia, GS: Gansu, SH': Shaanxi, SH: Shanxi, HB: Hebei, and IM: Inner Mongolia). (c) County-level NO_X AEIs in 2018 (black line, shown on a logarithmic scale) and relative changes in county-level AEIs from 2018 to 2024 (red line) as a function of urbanization rates (URs). The data are shown after moving average of 50 counties (denoted as 50-county moving average) ranked by URs. The gray shadow area denotes the interquartile range of the AEIs in 2018 within the 50-county moving window; and the red shadow area

https://doi.org/10.1021/acs.est.6c11406
Environ. Sci. Technol. XXXX, XXX, XXX−XXX

Downloaded from pubs.acs.org/esthag/article-pdf/doi/10.1021/acs.est.6c11406/6919082S/acs.est.6c11406.pdf by PEKING UNIV user on 19 November 2026

Figure 5. continued

denotes the interquartile range of the relative AEI changes within the 50-county moving window. The linear correlations between URs and AEIs (without logarithmic transformation) and between URs and relative AEI changes after 50-county moving average are also shown.

populous urban areas dominated by the tertiary sector, such as Longhua District in Shenzhen City (Figure 4).

By contrast, the top 10% emitting counties contribute 33.8 ± 0.7% of the national total in summer 2024; and over half of them (159 out of 285) are located in western China. These high-emitting counties in western China generally cover large areas with scattered industrial activities and long-distance road transportation, leading to high county-level emissions. Among them, Yizhou District in southern Hami City (marked in Figure 4), has the highest NO_X emission at 13.8 ± 1.9 × 10^4 Ton a^{-1}. Yizhou District is a growing center of coal mining and a key transportation hub linking Xinjiang Province with eastern China. In contrast, in eastern China, high-emitting counties tend to have small areas, dense population, and high per-unit-area emissions, particularly within the major city clusters like the North China Region (NRC) and the Yangtze River Delta (YRD) (Figure 4).

Notable contrasts are also observed across counties within a given province-level or prefecture-level city. For example, of the 16 county-level urban districts in Shanghai City (Figure 4), the six inner core districts exhibit very low emissions, totaling only 0.15 ± 0.07 × 10^4 Ton a^{-1} in summer 2024. In contrast, their adjacent outer districts, Baoshan and Pudong New Area, show 15−40 times more emissions at 2.43 ± 0.39 × 10^4 and 6.05 ± 0.87 × 10^4 Ton a^{-1}, respectively. Three of the six inner districts rank within the lowest 10% nationwide in terms of emission, whereas four of the ten outer districts belong to the highest 10%. This sharp contrast mainly reflects the functional zoning in Shanghai, with the inner districts dominated by residential and commercial use and the outer districts hosting industries and facilities with much higher emissions. Previous studies for a few cities have also found similar mismatches between city centers and prominent emission hotspots.[18,58]

3.2. Amplified Emission Reductions in More Urbanized Counties

From 2018 to 2024, the total anthropogenic NO_X emissions over mainland China decrease by 30.7 ± 8.3%. Year-to-year emission declines are stable during 2018−2024, except for the rebounds from 2022 to 2023 (Figure S10). These rebounds are likely associated with the lifting of COVID-19 restrictions in early 2023. Compared to county-level urban districts and cities, stronger rebounds occur in the 1,470 less-urbanized counties. This suggests that anthropogenic air pollution in these regions might be more sensitive to short-term socio-economic disruptions. In contrast, the impacts of the COVID-19 outbreak in 2020 are not evident in these summertime emission results. This is because the outbreak and associated lockdown occurred in winter-spring 2020, and by summer 2020 its effect had been dominated by the long-term emission trend.[20]

In order to characterize county-level emission changes and eliminate the effect of great cross-county heterogeneity in area, here we adopt areal emission intensity (AEI, i.e., emission per unit area) for further analysis. County-level total emissions are not used here because, given the substantial variability in county area, larger county-total emission does not necessarily correspond to a higher local ambient pollution burden. By contrast, under comparable meteorological and chemical conditions, a higher AEI typically indicates a higher local ambient pollution burden. It should also be noted that AEI does not fully represent population exposure or associated health impacts, which also depend on population distribution and inter-regional atmospheric transport.

Figure 5a shows the county-level AEIs in 2018. AEIs exhibit a more pronounced spatial clustering pattern than county-level emission amounts (Figure 4), after the effect of area is removed. For example, the AEI hotspots in Inner Mongolia and Xinjiang in the northwest are much less obvious than the emission hotspots shown in Figure 4. Yizhou District, which shows the highest county-level NO_X emission in both 2018 and 2024, exhibits a moderate AEI of 0.16 ± 0.02 kg km^{-2} h^{-1} (or at the 14th percentile) in 2018 and 0.20 ± 0.03 kg km^{-2} h^{-1} (or at the 29th percentile) in 2024. Still, the AEI ranges by several orders of magnitude across the counties (with a 10th−90th percentile range of 0.11−2.81 kg km^{-2} h^{-1} and the peak value at 22.6 kg km^{-2} h^{-1} in 2018).

In 2018, the cross-county variation of AEIs is positively correlated with the spatial disparity in urbanization rates (black line in Figure 5c, R = 0.77, P-value <0.01), after moving average of every 50 counties ordered by URs (hereinafter the same). Consistent with the distribution of URs (Figure S9), eastern counties have higher AEIs than those in the west. The AEIs are particularly large within several major cities in the NRC and YRD regions (Figure 5a), which are among the most urbanized regions in China. Here the moving average is applied to suppress county-specific variability (such as resource endowments, energy and industrial structures, and transportation preferences) not fully caused by urbanization, and to better reveal the underlying trend across urbanization levels. The observed relationship remains consistent for different moving-window sizes (10 and 25 counties, Figure S11).

From 2018 to 2024, about 84.1 ± 7.3% of counties experience AEI reductions (Figure 5b) whereas the remaining 452 counties experience increases. The cross-county variation in AEI changes is strongly negatively correlated with the spatial disparity in URs (red line in Figure 5c, R = −0.80, P-value <0.01). Weaker declines and even increases of AEIs occur in the counties with the lowest URs, which are mainly in the west and northeast with low AEIs in 2018. Consistently, a negative correlation is observed between the county-level AEIs in 2018 and their relative changes (R = −0.71, P-value <0.01), that is, the higher the AEI in 2018, the greater the decline from 2018 to 2024.

The observed correlations between UR, AEI and AEI change likely reflect inter-regional differences in how economic development demands and emission control efforts are balanced in counties at different stages of urbanization. Counties with higher URs are more likely to be targeted for greater emission reduction. For example, the Beijing-Tianjin-Hebei region (BTH), the YRD and the Fenhe-Weihe Plain (FWP) are the three "key regions" listed in the second-phase (covering 2015−2020) and third-phase (2020−2025) of national air pollution control policies.[2,3] And their average URs are 71.9%, 74.7%, and 63.8%, respectively, compared to the median value in the other regions at 49.7%. From 2018 to

Downloaded from pubs.acs.org/esthag/article-pdf/doi/10.1021/acs.est.6c11406/6919082S/acs.est.6c11406.pdf by PEKING UNIV user on 19 November 2026

https://doi.org/10.1021/acs.est.6c11406
Environ. Sci. Technol. XXXX, XXX, XXX−XXX

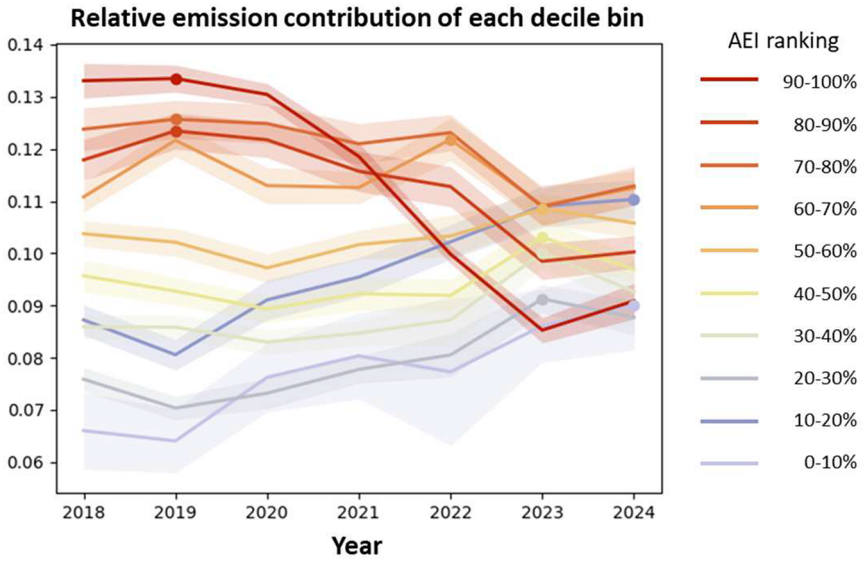


Figure 6. The narrowing gap of emission contributions. Relative contributions of NO_X emissions from counties in each decile bin ranked by county-level AEI in 2018. Dots on the curves denote the peak years of the relative contributions of each decile bin. The shaded areas indicate the 1-σ uncertainties derived from the Monte Carlo tests.

2024, these key regions experience emission reductions of 37.9 ± 8.5%, 42.9 ± 6.6%, and 33.5 ± 7.6%, respectively, compared with the collective decrease by 27.6 ± 8.8% in the other regions.

In contrast to the widespread emission reductions during the years, scattered emission increases mainly occur in western China. For example, a notable emission-increasing cluster is observed in the northwest (marked as EIC in Figure 5b). The EIC consists of 98 counties encompassing parts of Hebei, Shanxi, Shaanxi, Gansu, Ningxia, Xinjiang and Inner Mongolia provinces. The total NO_X emissions from EIC increase by 35.3 ± 15.5%, which likely reflects a local prioritization of economic development over emission control, consistent with its relatively low UR (46.9%) and AEI (0.16 ± 0.02 kg km^{-2} h^{-1} in 2018). During this period, EIC experiences rapid expansion of local mining, becomes a major supplier of electricity to other provinces, and receives nearly doubled number of tourists passing through this region to visit Xinjiang.[59,60]

These differences in AEI changes across the counties result in narrowed gaps in the relative emission contributions (to the national total) between high- and low-AEI counties from 2018 to 2024. Figure 6 illustrates the temporal changes in relative emission contribution from each decile bin of the 2,842 counties ranked in ascending order of AEIs in 2018. Clearly, the gap in relative emission contributions among the 10 decile bins keeps narrowing throughout the years. In particular, counties in the last decile bin (with the highest 10% AEIs in 2018) experience the greatest emission decline by 52.7 ± 4.4%, from 3.45 ± 0.45 × 10^6 Ton a^{-1} in 2018 to 1.63 ± 0.25 × 10^6 Ton a^{-1} in 2024. These counties contribute 13.3 ± 0.7% of the national total emissions in 2018, which is higher than the contribution from any other decile bin (Figure 6). By 2024, however, their contribution drops to 9.1 ± 0.8% only. Meanwhile, the contribution from the first decile bin (with the lowest AEIs in 2018) rises from 6.6 ± 0.3% in 2018 to 9.0 ± 0.3% in 2024. By 2024, the relative contributions from the ten individual decile bins become comparable (between 8.7% and 11.3%). Such evolving contrast between high- and low-AEI counties aligns with the faster emission declines observed in more urbanized counties (Figure 5c).

3.3. Decoupling of Emission and Economy

We further examine how county-level NO_X emissions and their temporal changes are related to economic development for counties at different UR levels. For this purpose, we obtain gross domestic product (GDP) data from 2018 to 2024 for 1,779 counties from their Statistical Yearbooks;[60] the GDP data are not available for other counties. In 2018, these 1,779 counties contribute 60.4% of the national GDP, and their NO_X emissions contribute 62.9 ± 0.4% of the national total. The counties with and without available GDP data do not show significant systematic difference in urbanization rate (0.65 versus 0.66), and the fractions of emission-increasing counties are also comparable between the two groups (16.5% versus 14.9%; Table S3). These results suggest broad representativeness of the 1,779 counties with available GDP data. We also obtain population density data in 2020[53] to facilitate the analysis.

Cross-county emission disparities lead to weak spatial relationships between NO_X emissions and both GDP and population. Across the 1,779 counties in 2018, the spatial correlation between county-level emissions and GDP is only 0.18, compared with 0.45 at the prefectural city level. By 2024, the correlation further declines to 0.10 at the county level and 0.34 at the city level. Similarly, the spatial correlation between emissions and population is 0.18 across counties and 0.54 across prefectural cities in 2018, further decreasing to 0.07 and 0.40, respectively, by 2024. These scale-dependent correlations reflect substantial heterogeneity in industry and functional specialization among counties within the same prefectural city, which leads to the weak correlations at the county level. The continued weakening of these correlations over time suggests an increasing extent of spatial decoupling between economic volume and emission.

To quantify the temporal progress of emission-economy decoupling, we analyze the economic emission intensity (EEI, defined as NO_X emission per unit GDP at constant 2020 prices). From 2018 to 2024, the average EEI of these 1,779

Downloaded from pubs.acs.org/esthag/article-pdf/doi/10.1021/acs.est.6c11406/6919082S/acs.est.6c11406.pdf by PEKING UNIV user on 19 November 2026

https://doi.org/10.1021/acs.est.6c11406
Environ. Sci. Technol. XXXX, XXX, XXX−XXX

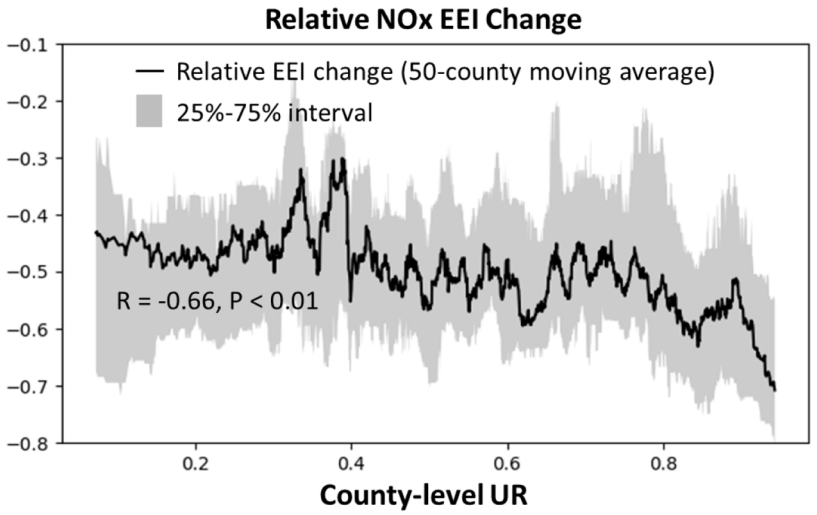


Figure 7. Emission-economy decoupling related to urbanization level. Relative NO_X EEI changes, driven by GDP growth and emission reductions, as a function of URs. The data are shown after moving average of 50 counties ranked by URs. The shadow areas denote the interquartile range within the 50-county moving window. The observed relationship remains qualitatively consistent when other moving-window sizes are used (10 and 25, Figure S11).

counties declines by 48.7 ± 6.3%, from 0.28 ± 0.04 to 0.15 ± 0.02 g CNY^{-1}. According to the definitions of "decoupling" from the Organization for Economic Co-operation and Development (OECD),[61] among these 1,779 counties, 76.7 ± 7.1% (1,364 counties) reach absolute decoupling (i.e., with increasing GDP but decreasing emission). In these counties, NO_X emissions decrease by 39.8 ± 3.9%, while GDP grows by 39.1%, with both contributing comparably to the observed decoupling. Besides, another 9.4 ± 3.9% (168 counties) achieve relative emission-economy decoupling (i.e., with decreasing EEI but increasing emission). Although emissions increase in these counties (20.0 ± 1.7%), their rapid GDP growth (57.3%) dominates the net effect, resulting in EEI declines. Collectively, 86.1 ± 3.3% (1,532 counties) achieve emission-economy decoupling to varying extents. Counties exhibiting absolute decoupling have a higher UR than those with relative decoupling (0.64 versus 0.59) on average, and they also have substantially higher baseline AEI in 2018 than the latter by a factor of 1.95.

For the counties showing relative decoupling, their average GDP increase (57.3%) is larger than the national average (34.5%).[60] These counties are mainly located in three major regions (northwest, south, and east, Figure S12). In northwestern China, the relative-decoupling counties are mainly located within the EIC identified in Section 3.2, particularly in Gansu, Xinjiang, and Inner Mongolia. In this region, the growth of GDP and emissions is likely associated with the rapid expansion of coal-fired power generation, coal production and freight transportation (e.g., coal shipment[62]). During 2018−2024, coal production and thermal power generation in these three provinces increase by 64.5% and 58.9%,[60] respectively. Increasing tourism,[60] especially self-drive travel, may also play an important role. Another major cluster is located in the south, including Yunnan, Guizhou, Sichuan, Guangxi, and Guangdong provinces. Overseas export values increased by 85.1% in Yunnan, Guizhou, Sichuan and Guangxi, substantially exceeding the national average (55.0%),[60] while Guangdong provides convenient coastal gateways. The associated expansion of mining, manufacturing and freight transportation may have contributed to both economic growth and emissions increases. In the third cluster encompassing Anhui and Zhejiang provinces in eastern China, similar export growth is also observed, contributing to their economic and emission growth.

In contrast, counties in China's four largest megacities (Beijing, Shanghai, Guangzhou, and Shenzhen cities) exhibit a clear absolute decoupling pattern. This includes the previously discussed inner districts of Shanghai and Longhua District in Shenzhen, all of which achieved absolute decoupling. These counties reach an average UR of 0.90. Their cumulative GDP growth during 2018−2024 (33.2%)[60] is close to the national average, but their NO_X emission declines by 38.5 ± 8.7% due to the implementation of stringent environmental regulations,[63] including the promotion of electric vehicles[64] and tertiary sector,[65] phase-out of polluting industries,[66] and clean-energy transition.[67]

Across the 1,779 counties, relative EEI changes exhibit an overall negative correlation with URs (R = −0.66, P-value <0.01; Figure 7). This means that the emission-economy decoupling tends to be stronger in more urbanized counties. Such enhanced decoupling is primarily driven by larger emission reductions in the counties with higher URs as shown in Figure 5c. For instance, counties with URs exceeding 0.9 experience a 53.5 ± 7.9% reduction in NO_X emissions, much larger than the 30.3 ± 8.5% reduction in the other counties. In contrast, GDP in these highly urbanized counties increases by 37.4%, slightly larger than the 34.2% growth in the other counties. This contrast may reflect a stronger emphasis on pollution mitigation than on maximizing economic growth in these highly urbanized counties, thereby facilitating more pronounced emission-economy decoupling.

The correlation between EEI changes and URs is also observed across county types including urban districts, county-level cities and the other counties. Urban districts and county-level cities have URs of 0.78 and 0.63, respectively. They occupy 9.8% and 16.5% of the 1,779-county total land area, accommodate 44.6% and 17.3% of the population, and contribute 29.5 ± 0.3% and 20.4 ± 0.2% of the emissions in 2018, while accounting for 57.5% and 17.5% of the GDP. Their high population densities (634.1 and 145.9 km^{-2} on

https://doi.org/10.1021/acs.est.6c11406
Environ. Sci. Technol. XXXX, XXX, XXX−XXX

Downloaded from pubs.acs.org/esthag/article-pdf/doi/10.1021/acs.est.6c11406/6919082S/acs.est.6c11406.pdf by PEKING UNIV user on 19 November 2026

average, compared to 71.8 km^{-2} in the other county-level administrative units) provide favorable conditions for the expansion of the tertiary sector and lower tolerance for air pollution.[68] From 2018 to 2024, EEI decreases by 53.0 ± 6.0% (from 0.15 ± 0.02 to 0.07 ± 0.01 g CNY^{-1}) in the urban districts and by 50.8 ± 5.7% (from 0.33 ± 0.05 to 0.16 ± 0.03 g CNY^{-1}) in the county-level cities. By comparison, the other less urbanized counties have a much lower average UR of 0.49, and their EEI is much higher (0.57 ± 0.09 g CNY^{-1}) in 2018 and exhibits a relatively weaker reduction by 46.0 ± 6.5% from 2018 to 2024. This contrast in EEI changes across county types is consistent with their changes in emission amounts (Figure S10), underscoring the dominant role of emission control in emission-economy decoupling across Chinese counties.

3.4. Consistency with Ground-Based Pollution Measurements

The spatiotemporal characteristics of county-level emissions are consistent with the near-surface NO_2 concentrations measured by MEE ground-based air quality monitoring sites, which are independent of our emission inversion. We compile the ground-based NO_2 observations from 676 counties with valid measurements from MEE sites (see data quality control in Section 2.3.1) and examine the changes in county-level surface NO_2 concentrations. We find that the summer average NO_2 concentrations across the counties in 2018 are also strongly positively correlated with the corresponding URs (R = 0.97, P-value <0.01); and the relative changes in county-level surface NO_2 concentrations from 2018 to 2024 are negatively correlated with county-level URs (R = −0.84, P-value <0.01, Figure S3a). This means that more urbanized counties tend to experience heavier ambient pollution in the earlier year but a large extent of pollution alleviation throughout the period, which is similar to the results for AEIs. In addition, the differences in average NO_2 concentrations across the decile bins (ranked by county-level AEIs in 2018) of the 676 counties exhibit convergence from 2018 to 2024, with their normalized standard deviation decreasing from 20.6% to 15.3% (Figure S3b), consistent with the convergence of emission contributions (Figure 6). Furthermore, the NO_2 concentration changes from one year to another, including the rebound from 2022 to 2023, are consistent with the emission changes (Figure S4).

4. DISCUSSION

This study characterizes recent county-level anthropogenic air pollution characteristics in 2,842 counties across mainland China, enabled by our satellite-based NO_X emission inversion to break through the bottlenecks of conventional emission inventories in timeliness and spatial resolution. By resolving significant county-level variability in emission amounts, AEIs and EEIs, our study moves beyond previous province- and city-level analyses[10,17] toward a substantially finer spatial scale, revealing spatially detailed patterns in the outcome of recent economic-environmental policy implementation in China.

Our analysis shows that the three-phased national strategies[1−3] have achieved remarkable progress toward greener development with stronger emission-economy decoupling as urbanization takes place in China. From 2018 to 2024, the national total summertime NO_X emissions decrease by 30.7 ± 8.3% despite the continuous economic growth, resulting in a substantial alleviation of the national emission burden of economic growth (represented by EEI) by 48.7 ± 6.3%. About 84.1 ± 7.3% of counties experience emission reductions, 86.1 ± 3.3% achieve emission-economy decoupling to varying extents, and 76.7 ± 7.1% reach absolute decoupling. Such emission-economy decoupling is stronger in more urbanized counties where the AEI is generally higher in 2018. These county-level decoupling patterns highlight the importance of resolving emissions at high resolution.

Despite the small seasonal variability indicated by the inventories and the limited interannual variation in the summertime fraction of annual NO_X emissions (Figure S1), extrapolating the inferred summertime trends to annual trends still relies on stable seasonality in actual emissions. A potentially important bias is wintertime heating in northern China. However, heating contributed relatively little to local annual NO_X emissions (e.g., ∼4% from distributed residential coal heating,[69] and ∼7% based on our estimate including distributed heating, centralized heating and 50% of combined heat and power boilers in the BTH region in 2020[70,71]). Moreover, heating-related NO_X emissions have declined rapidly with the control of residential coal combustion and the expansion of cleaner centralized heating systems.[72,73] In the NRC, reductions in residential coal-burning NO_X have even outpaced the overall decline in anthropogenic NO_X emissions.[73] Most counties in North China and Northeast China are also identified as achieving absolute emission-economy decoupling in our analysis. In contrast, the emission increases observed in northwestern China are, as discussed above, primarily associated with industrial and power-sector activities and related transportation emissions. Therefore, seasonal differences are not likely to substantially affect the county-level emission-economy decoupling patterns in this study.

A comparison with widely used inventories including MEIC v2.0, CEDS v2025−04 and EDGAR v8.1 (Figures S13−S15) further demonstrates the capability of our satellite-based inversion to complement them with fine-scale information. In particular, the convergence of relative emission contributions across counties with different initial AEI levels is not evident in these inventories. Likewise, the relationship between emission-economy decoupling and urbanization level is substantially weaker, or even reversed, in the inventory-based estimates. These discrepancies may arise from uncertainties in emission factors adopted by the inventories, which may be outdated and may not properly represent county-level characteristics, as well as limitations in county-level activity statistics that can lead to emission misallocation, such as emissions associated with cross-regional transportation.[74] The relatively coarse spatial resolution of emission inventories may also smooth out county-scale emission characteristics.

The stronger emission-economy decoupling observed in more urbanized counties is likely associated with differences in industrial structure and dominant emission mitigation pathways across the stages of urbanization. In more urbanized counties, economic growth increasingly relies on service-oriented and high-tech industries, alongside the phase-out of polluting industries, facilitating stronger absolute decoupling, as demonstrated by previous case studies.[75,76] In contrast, less-urbanized counties, especially in northwestern China, remain more dependent on secondary and resource-based industries.[77,78] Their emission reductions rely more heavily on end-of-pipe emission controls, which have been identified as a primary driver of China's overall emission reductions.[79] These different mitigation pathways contribute to the relatively weaker emission-economy decoupling in less-urbanized

Downloaded from pubs.acs.org/esthag/article-pdf/doi/10.1021/acs.est.6c11406/6919082S/acs.est.6c11406.pdf by PEKING UNIV user on 19 November 2026

https://doi.org/10.1021/acs.est.6c11406
Environ. Sci. Technol. XXXX, XXX, XXX−XXX

counties. As such, the relative contribution of pollutant emissions has been rapidly transitioning from the well-studied eastern regions toward less-urbanized counties. In the future, continued urbanization and clean-energy deployment[80,81] will be essential for emission control and achieving more sustained emission-economy decoupling, particularly in the resource-based and energy-supplying regions.

Despite the overall remarkable emission reductions, new challenges have emerged for future air quality management. These emerging challenges are much more evident at finer spatial scales. During 2018−2024, emission growth does not occur at the provincial level, compared with emission growth in 8.2% of prefecture-level cities and 15.9% of counties. These results highlight the increasing importance of strengthening emission control in these counties with worsening pollution burden. This could be done by improved monitoring of emerging emission sources,[17] enhancement of end-of-pipe control, industrial upgrade, and switching toward cleaner energy and transportation, supported in part by financial, technical and knowledge support from the more urbanized (and typically wealthier) eastern counties. This effort in turn requires county-scale emission characterization to support pollution tracking and mitigation.

Ground-based monitoring must be updated to keep pace with the emerging changes in emission patterns. Among the 452 counties experiencing emission growth, 71.7% remain uncovered by the existing national-level monitoring network. About 56.9% of the 452 counties are less-urbanized counties (other than county-level cities and urban districts). Among the less-urbanized counties, MEE monitoring covers only 2.4% of counties, compared with 15.9% for county-level cities and 81.8% for urban districts. This situation is worsened by a substantial east−west gap in the coverage of MEE monitoring. In western China (region shown in Figure 4), only 24.2% of counties contain MEE sites, compared with 37.7% in eastern China. Moreover, counties in western China generally cover larger areas, especially in XJ and IM where notable emission increases are shown, further impacting the spatial representativeness of MEE sites. Thus, future development of ground-based monitoring network should place greater emphasis on the evolving spatial distribution of emissions, particularly newly emerging emission hotspots and northwestern energy-supplying counties with increasing emissions identified by satellite-based inversion. To this end, satellite-based emission inversions, integrated with bottom-up inventories and ground-based monitoring, can better capture the redistribution of polluting industries, from individual factory relocations to broader geographical shifts in industrial capacity, while supporting more adaptive monitoring-network planning and county-specific mitigation strategies.

■ ASSOCIATED CONTENT

Supporting Information

The Supporting Information is available free of charge at https://pubs.acs.org/doi/10.1021/acs.est.6c11406.

Summer NO_X emission ratios in each year based on inventories (Figure S1); changes in NO_X emissions from soil and open fires (Figure S2); county-level surface NO_2 concentrations based on MEE monitoring, their relative changes alongside urbanization rates, and changes in decile bins ranked by county-level AEI (Figure S3); changes in NO_X emissions and surface NO_2 concentrations in counties with valid MEE monitoring (Figure S4); spatial correlation between changes in near-surface NO_2 in June based on MEE measurements and CTM simulations (Figure S5); evaluation of PHLET-derived NO_X emission using GEOS-Chem with MEIC v2.0 (Figure S6); domains for WRF-Chem simulations (Figure S7); comparisons with in situ flux measurements from an eddy-covariance tower (Figure S8); county-level urbanization rates in 2020 (Figure S9); NO_X emission variations for each county type (Figure S10); sensitivity tests for different moving-window sizes (Figure S11); distribution of counties with different extents of emission-economy decoupling (Figure S12); county-scale emission characteristics derived from MEIC (Figure S13); county-scale emission characteristics derived from CEDS (Figure S14); county-scale emission characteristics derived from EDGAR (Figure S15); statistical evaluation of GEOS-Chem simulations driven by the MEIC v1.4 and PHLET-derived NO_X emissions (Table S1); statistical comparison of county-level NO_X emissions between the CAQIEI and PHLET-derived emissions, and between the CAQIEI and bottom-up inventories (Table S2); comparison of urbanization and emission characteristics between counties with and without available GDP data (Table S3) (PDF)

■ AUTHOR INFORMATION

Corresponding Author

Jintai Lin − *Laboratory for Climate and Ocean-Atmosphere Studies, Department of Atmospheric and Oceanic Sciences, School of Physics, Peking University, Beijing 100871, China; Institute of Carbon Neutrality, Peking University, Beijing 100871, China;* orcid.org/0000-0002-2362-2940; Email: linjt@pku.edu.cn

Authors

Hao Kong − *Laboratory for Climate and Ocean-Atmosphere Studies, Department of Atmospheric and Oceanic Sciences, School of Physics, Peking University, Beijing 100871, China;* orcid.org/0000-0001-5038-2914

Sijie Wang − *Laboratory for Climate and Ocean-Atmosphere Studies, Department of Atmospheric and Oceanic Sciences, School of Physics, Peking University, Beijing 100871, China;* orcid.org/0009-0007-5688-1993

Ruijing Ni − *Sichuan Academy of Environmental Policy and Planning, Chengdu, Sichuan 610093, China*

Yuhang Zhang − *Laboratory for Climate and Ocean-Atmosphere Studies, Department of Atmospheric and Oceanic Sciences, School of Physics, Peking University, Beijing 100871, China*

Mengying Wang − *Laboratory for Climate and Ocean-Atmosphere Studies, Department of Atmospheric and Oceanic Sciences, School of Physics, Peking University, Beijing 100871, China*

Chenghao Xu − *Laboratory for Climate and Ocean-Atmosphere Studies, Department of Atmospheric and Oceanic Sciences, School of Physics, Peking University, Beijing 100871, China*

Complete contact information is available at: https://pubs.acs.org/10.1021/acs.est.6c11406

https://doi.org/10.1021/acs.est.6c11406
Environ. Sci. Technol. XXXX, XXX, XXX−XXX

Downloaded from pubs.acs.org/esthag/article-pdf/doi/10.1021/acs.est.6c11406/6919082S/acs.est.6c11406.pdf by PEKING UNIV user on 19 November 2026

Author Contributions

J.L. conceived the research. J.L. and H.K. designed the research. H.K. performed the data processing, model development, and simulation. Y.Z. and S.W. contributed to model development and data processing. R.N. contributed to the analysis of the results. M.W. contributed to the retrieval of POMINO-TROPOMI NO_2 VCDs. C.X. contributed to the processing of MEE data. H.K. and J.L. analyzed the results and wrote the paper. All authors commented on the manuscript.

Notes

The authors declare no competing financial interest.

■ ACKNOWLEDGMENTS

This research is supported by the National Key Research and Development Program of China (grant no. 2023YFC3705802), the National Natural Science Foundation of China (grant no. 42430603), the China Postdoctoral Science Foundation (grant nos. 2025T180079 and 2024M760087). The GEOS-FP data used in this study are provided by the Global Modeling and Assimilation Office (GMAO) at NASA Goddard Space Flight Center. We thank Dr. Yiwen Hu for assistance in evaluating the emission inversion. We thank for the technical support of the National Large Scientific and Technological Infrastructure "Earth System Numerical Simulation Facility" (https://cstr.cn/31134.02.EL).

■ REFERENCES

(1) China's State Council *Action Plan for Air Pollution Prevention and Control*; 2013. https://www.gov.cn/zwgk/2013-09/12/content_2486773.htm. (accessed 2026−10−21).

(2) China's State Council. *Three-Year Action Plan to Win the Battle for Blue Skies*; 2018, https://www.gov.cn/zhengce/content/2018-07/03/content_5303158.htm. (accessed 2026−10−21).

(3) China's State Council. *Action Plan for Continuous Improvement of Air Quality*; 2023, https://www.mee.gov.cn/zcwj/gwywj/202312/t20231208_1058492.shtml. (accessed 2026−10−21).

(4) Geng, G.; Zhang, Q.; Martin, R.; Lin, J.; Huo, H.; Zheng, B.; Wang, S.; He, K. Impact of spatial proxies on the representation of bottom-up emission inventories: A satellite-based analysis. *Atmos. Chem. Phys.* **2017**, *17*, 4131−4145.

(5) Zheng, B.; Cheng, J.; Geng, G.; Wang, X.; Li, M.; Shi, Q.; Qi, J.; Lei, Y.; Zhang, Q.; He, K. Mapping anthropogenic emissions in China at 1 km spatial resolution and its application in air quality modeling. *Sci. Bull.* **2021**, *66* (6), 612−620.

(6) Guo, W.; Shi, Y.; Liu, Y.; Su, M. CO2 emissions retrieval from coal-fired power plants based on OCO-2/3 satellite observations and a Gaussian plume model. *J. Clean. Prod.* **2023**, *397*, 136525.

(7) Xu, C.; Lin, J.; Wang, S.; Kong, H.; Zhang, Y.; Yun, Y.; Ren, F.; Wang, M.; Tan, W.; Wang, J.; et al. Satellite-detected nitrogen oxides emission changes from power plant dynamics in North China. *Environ. Res. Lett.* **2026**, *21*, 154012.

(8) Liu, M.; Ge, Y. The nexus between poverty reduction and carbon emissions: Insights from Hubei, China during the Targeted Poverty Alleviation Period. *Geogr. Sustainability* **2025**, *6* (4), 100308.

(9) Li, L.; Zhao, Q.; Zhang, J.; Li, H.; Liu, Q.; Li, C.; Chen, F.; Qiao, Y.; Han, J. Bottom-up emission inventories of multiple air pollutants from open straw burning: A case study of Jiangsu province, Eastern China. *Atmos. Pollut. Res.* **2019**, *10* (2), 501−507.

(10) Kong, H.; Lin, J.; Ni, R.; Du, M.; Wang, J.; Chen, L.; Xu, C.; Yan, Y.; Weng, H.; Zhang, Y. Satellite detected weak decline of nitrogen oxides emissions in economically small cities of China. *Environ. Res. Lett.* **2025**, *20* (7), 074046.

(11) Kong, L.; Tang, X.; Wang, Z.; Zhu, J.; Li, J.; Wu, H.; Wu, Q.; Chen, H.; Zhu, L.; Wang, W.; et al. Changes In Air Pollutant Emissions In China During Two Clean-Air Action Periods Derived From The Newly Developed Inversed Emission Inventory For Chinese Air Quality (CAQIEI). *Earth Syst. Sci. Data* **2024**, *16*, 4351−4387.

(12) Luo, H.; Tang, X.; Wu, H.; Kong, L.; Wu, Q.; Cao, K.; Song, Y.; Luo, X.; Wang, Y.; Zhu, J.; et al. The Impact of the Numbers of Monitoring Stations on the National and Regional Air Quality Assessment in China During 2013−18. *Adv. Atmos. Sci.* **2022**, *39* (10), 1709−1720.

(13) Du, L.; Wang, R.; Wang, Z. Cutting ties with local bureaucrats: How does the environmental vertical management reform affect firm pollution in China? *J. Clean. Prod.* **2024**, *447*, 141432.

(14) Xu, S.-C.; Miao, Y.-M.; Gao, C.; Long, R.-Y.; Chen, H.; Zhao, B.; Wang, S.-X. Regional differences in impacts of economic growth and urbanization on air pollutants in China based on provincial panel estimation. *J. Clean. Prod.* **2019**, *208*, 340−352.

(15) Qu, Z.; Henze, D. K.; Worden, H. M.; Jiang, Z.; Gaubert, B.; Theys, N.; Wang, W. Sector-Based Top-Down Estimates of NOx, SO2, and CO Emissions in East Asia. *Geophys. Res. Lett.* **2022**, *49* (2), No. e2021GL096009.

(16) Kong, Y.; Zheng, B.; Liu, Y. Tracking daily NOx emissions from an urban agglomeration based on TROPOMI NO2 and a local ensemble transform Kalman filter. *Atmos. Chem. Phys.* **2025**, *25*, 5959−5976.

(17) Kong, H.; Lin, J.; Chen, L.; Zhang, Y.; Yan, Y.; Liu, M.; Ni, R.; Liu, Z.; Weng, H. Considerable Unaccounted Local Sources of NOx Emissions in China Revealed from Satellite. *Environ. Sci. Technol.* **2022**, *56* (11), 7131−7142.

(18) Kong, H.; Lin, J.; Zhang, R.; Liu, M.; Weng, H.; Ni, R.; Chen, L.; Wang, J.; Yan, Y.; Zhang, Q. High-resolution (0.05° × 0.05°) NO x emissions in the Yangtze River Delta inferred from OMI. *Atmos. Chem. Phys.* **2019**, *19* (20), 12835−12856.

(19) Beirle, S.; Borger, C.; Dörner, S.; Li, A.; Hu, Z.; Liu, F.; Wang, Y.; Wagner, T. Pinpointing nitrogen oxide emissions from space. *Sci. Adv.* **2019**, *5* (11), No. eaax9800.

(20) Zheng, B.; Geng, G.; Ciais, P.; Davis, S. J.; Martin, R. V.; Meng, J.; Wu, N.; Chevallier, F.; Broquet, G.; Boersma, F.; et al. Satellite-based estimates of decline and rebound in China's CO_2 emissions during COVID-19 pandemic. *Sci. Adv.* **2020**, *6* (49), No. eabd4998.

(21) Geffen, J. H. G. M. V.; Eskes, H. J.; Boersma, K. F.; Veefkind, J. P. *TROPOMI ATBD of the total and tropospheric NO_2 data products, 2.9.0*; Royal Netherlands Meteorological Institute (KNMI): 2025. (accessed 2026−10−21).

(22) Lin, J. T.; Liu, M. Y.; Xin, J. Y.; Boersma, K. F.; Spurr, R.; Martin, R.; Zhang, Q. Influence of aerosols and surface reflectance on satellite NO_2 retrieval: seasonal and spatial characteristics and implications for NOx emission constraints. *Atmos. Chem. Phys.* **2015**, *15* (19), 11217−11241.

(23) Lin, J. T.; Martin, R. V.; Boersma, K. F.; Sneep, M.; Stammes, P.; Spurr, R.; Wang, P.; Van Roozendael, M.; Clémer, K.; Irie, H. Retrieving tropospheric nitrogen dioxide from the Ozone Monitoring Instrument: effects of aerosols, surface reflectance anisotropy, and vertical profile of nitrogen dioxide. *Atmos. Chem. Phys.* **2014**, *14* (3), 1441−1461.

(24) Liu, M.; Lin, J.; Boersma, K. F.; Pinardi, G.; Wang, Y.; Chimot, J.; Wagner, T.; Xie, P.; Eskes, H.; Van Roozendael, M.; et al. Improved aerosol correction for OMI tropospheric NO2 retrieval over East Asia: constraint from CALIOP aerosol vertical profile. *Atmos. Meas. Technol.* **2019**, *12* (1), 1−21.

(25) Liu, M.; Lin, J.; Kong, H.; Boersma, K. F.; Eskes, H.; Kanaya, Y.; He, Q.; Tian, X.; Qin, K.; Xie, P.; et al. A new TROPOMI product for tropospheric NO_2 columns over East Asia with explicit aerosol corrections. *Atmos. Meas. Technol.* **2020**, *13* (8), 4247−4259.

(26) Zhang, Y.; Lin, J.; Kim, J.; Lee, H.; Park, J.; Hong, H.; Van Roozendael, M.; Hendrick, F.; Wang, T.; Wang, P.; et al. A research product for tropospheric NO2 columns from Geostationary Environment Monitoring Spectrometer based on Peking University OMI NO2 algorithm. *Atmos. Meas. Technol.* **2023**, *16* (19), 4643−4665.

Downloaded from pubs.acs.org/esthag/article-pdf/doi/10.1021/acs.est.6c11406/6919082S/acs.est.6c11406.pdf by PEKING UNIV user on 19 November 2026

(27) Griffin, D.; Zhao, X.; McLinden, C. A.; Boersma, F.; Bourassa, A.; Dammers, E.; Degenstein, D.; Eskes, H.; Fehr, L.; Fioletov, V.; et al. High-Resolution Mapping of Nitrogen Dioxide With TROPOMI: First Results and Validation Over the Canadian Oil Sands. *Geophys. Res. Lett.* **2019**, *46* (2), 1049−1060.
(28) Eskes, H.; Eichmann, K. U.; Lambert, J. C.; Loyola, D.; Veefkind, P.; Dehn, A.; Zehner, C. *S5P Mission Performance Centre Nitrogen Dioxide [L2__NO2___] Readme, Version:01.03.00*; Royal Netherlands Meteorological Institute (KNMI): Netherlands, 2019.
(29) Wei, L.; Liu, S. C.; Tan, Z.; Ma, X.; Zhou, M.; Wei, W.; Zhang, J.; Zhang, Y.; Liu, R.; Lu, K. Atmospheric oxidation capacity at northern mid-latitude regions is reaching a turning point. *Nat. Sci. Rev.* **2026**, *13* (8), nwag178.
(30) Xue, R.; Wang, S.; Zhu, J.; Zhang, S.; Gu, C.; Yan, Y.; Jiang, Z.; Li, Q.; Ma, X.; Zou, Z.; et al. Increasing Urban OH Levels in China over the Past Decade. *Environ. Sci. Technol.* **2026**, *60* (21), 15185−15194.
(31) Weng, H.; Lin, J.; Martin, R.; Millet, D. B.; Jaeglé, L.; Ridley, D.; Keller, C.; Li, C.; Du, M.; Meng, J. Global high-resolution emissions of soil NOx, sea salt aerosols, and biogenic volatile organic compounds. *Sci. Data* **2020**, *7* (1), 148.
(32) Kaiser, J.; Heil, A.; Andreae, M.; Benedetti, A.; Chubarova, N.; Jones, L.; Morcrette, J.-J.; Razinger, M.; Schultz, M.; Suttie, M.; van der Werf, G. Biomass burning emissions estimated with a global fire assimilation system based on observed fire radiative power. *Biogeosciences* **2012**, *9* (1), 527−554.
(33) International GEOS-Chem User Community *geoschem/geos-chem: GEOS-Chem. 14.5.1.*; *Zenodo*, 2025. .
(34) Wu, F.; Hu, T.; Cao, J.; Guo, X.; Li, G.; Zhang, T.; Yang, Y.; Zhao, C.; Zhang, D. Active Nitrogen Cycle Driven by Solar Radiation in Clean Desert Air. *Earth's Future* **2022**, *10* (4), No. e2021EF002451.
(35) *Tencent. Tencent location big data* 2021, https://xingyun.map.qq.com/. (accessed 2023−02−13).
(36) Hsu, F.-C.; Baugh, K. E.; Ghosh, T.; Zhizhin, M.; Elvidge, C. D. DMSP-OLS Radiance Calibrated Nighttime Lights Time Series with Intercalibration. *Remote Sens.* **2015**, *7* (2), 1855−1876.
(37) Feng, X.; Xiu, C.; Bai, L.; Wen, Y. Urban Centrality and Influencing Factors in Jilin Province from the Perspective of Highway Traffic Flow. *Econ. Geogr.* **2019**, *39* (1), 64−72.
(38) Lin, H.; Long, M. S.; Sander, R.; Sandu, A.; Yantosca, R. M.; Estrada, L. A.; Shen, L.; Jacob, D. J. An Adaptive Auto-Reduction Solver for Speeding Up Integration of Chemical Kinetics in Atmospheric Chemistry Models: Implementation and Evaluation in the Kinetic Pre-Processor (KPP) Version 3.0.0. *J. Adv. Model. Earth Syst.* **2023**, *15* (2), No. e2022MS003293.
(39) Rienecker, M. M.; Suarez, M. J.; Todling, R.; Bacmeister, J.; Takacs, L.; Liu, H.-C.; Gu, W.; Sienkiewicz, M.; Koster, R. D.; Gelaro, R.et al.*GEOS-5 Data Assimilation System-Documentation Of Versions 5.0.1, 5.1.0, And 5.2.0*; National Aeronautics and Space Administration, Goddard Space Flight Center; 2008.
(40) Lin, J.-T.; McElroy, M. B. Impacts of boundary layer mixing on pollutant vertical profiles in the lower troposphere: Implications to satellite remote sensing. *Atmos. Environ.* **2010**, *44* (14), 1726−1739.
(41) Wesely, M. L. Parameterization of surface resistances to gaseous dry deposition in regional-scale numerical models. *Atmos. Environ.* **2007**, *41*, 52−63.
(42) Wang, Y.; Jacob, D. J.; Logan, J. A. Global simulation of tropospheric O3-NO x -hydrocarbon chemistry: 1. Model formulation. *J. Geophys. Res.: Atmos.* **1998**, *103* (D9), 10713−10725.
(43) Zhang, L.; Gong, S.; Padro, J.; Barrie, L. A size-segregated particle dry deposition scheme for an atmospheric aerosol module. *Atmos. Environ.* **2001**, *35* (3), 549−560.
(44) Lamsal, L. N.; Martin, R. V.; van Donkelaar, A.; Steinbacher, M.; Celarier, E. A.; Bucsela, E.; Dunlea, E. J.; Pinto, J. P. Ground-level nitrogen dioxide concentrations inferred from the satellite-borne Ozone Monitoring Instrument. *J. Geophys. Res.: Atmos.* **2008**, *113*, D16308.
(45) Liu, F.; van der A, R. J.; Eskes, H.; Ding, J.; Mijling, B. Evaluation of modeling NO2 concentrations driven by satellite-derived and bottom-up emission inventories using in situ measurements over China. *Atmos. Chem. Phys.* **2018**, *18* (6), 4171−4186.
(46) Skamarock, W. C.; Klemp, J. B.; Dudhia, J.; Gill, D. O.; Powers, J. G.*A Description Of The Advanced Research WRF Version 3. NCAR Technical Note Ncar/TN-475+str. June 2008. Mesoscale And Microscale Meteorology Division*; National Center for Atmospheric Research: Boulder; 2008.
(47) Li, Z.; Zang, Z.; Li, Q. B.; Chao, Y.; Chen, D.; Ye, Z.; Liu, Y.; Liou, K. N. A three-dimensional variational data assimilation system for multiple aerosol species with WRF/Chem and an application to PM2.5 prediction. *Atmos. Chem. Phys.* **2013**, *13* (8), 4265−4278.
(48) Zaveri, R. A.; Peters, L. K. A new lumped structure photochemical mechanism for large-scale applications. *J. Geophys. Res.: Atmos.* **1999**, *104* (D23), 30387−30415.
(49) Squires, F.; Nemitz, E.; Langford, B.; Wild, O.; Drysdale, W.; Acton, W.; Fu, P.; Grimmond, S.; Hamilton, J.; Hewitt, C.; et al. Measurements of traffic-dominated pollutant emissions in a Chinese megacity. *Atmos. Chem. Phys.* **2020**, *20* (14), 8737−8761.
(50) Zhang, X.; Yuan, B.; Huangfu, Y.; Liu, H.; Karl, T.; Chang, M.; Chen, S.; Song, T.; Lin, J.; Geng, G.; et al. Flux measurements of NOx, O3 and Ox: Emission characteristics, inventory validation and titration effects. *Environ. Pollut.* **2025**, *386*, 127213.
(51) Ministry of Civil Affairs of the People's Republic of China. *Measures for the Implementation of the Regulation on the Administration of Administrative Divisions*; 2019, https://www.gov.cn/zhengce/2019-12/11/content_5713162.htm. (accessed 2026−10−21).
(52) Xinliang, X. *Multi-year county-level administrative boundary data of China*; Resource And Environmental Science Data Platform. 2023.
(53) Ju, Y.; Liang, Y.; Kong, J.; Wang, X.; Wen, S.; Shang, H.; Wang, X. 100-m resolution Age-Stratified Population Estimation from the 2020 China Census by Township (ASPECT). *Sci. Data* **2025**, *12* (1), 1058.
(54) Pesaresi, M.; Schiavina, M.; Politis, P.; Freire, S.; Krasnodębska, K.; Uhl, J. H.; Carioli, A.; Corbane, C.; Dijkstra, L.; Florio, P.; et al. Advances on the Global Human Settlement Layer by joint assessment of Earth Observation and population survey data. *Int. J. Digital Earth* **2024**, *17* (1), 2390454.
(55) Liu, X.; Gao, X.; Wu, X.; Yu, W.; Chen, L.; Ni, R.; Zhao, Y.; Duan, H.; Zhao, F.; Chen, L.; et al. Updated Hourly Emissions Factors for Chinese Power Plants Showing the Impact of Widespread Ultralow Emissions Technology Deployment. *Environ. Sci. Technol.* **2019**, *53* (5), 2570−2578.
(56) Wang, Y.; Wang, H.; Zhang, B.; Liu, P.; Wang, X.; Si, S.; Xue, L.; Zhang, Q.; Wang, Q. High-resolution mapping of on-road vehicle emissions with real-time traffic datasets based on big data. *Atmos. Chem. Phys.* **2025**, *25*, 5537−5555.
(57) Lin, J.; McElroy, M.; Boersma, K. Constraint of anthropogenic NOx emissions in China from different sectors: A new methodology using multiple satellite retrievals. *Atmos. Chem. Phys.* **2010**, *10*, 63−78.
(58) Lonsdale, C. R.; Sun, K. Nitrogen oxides emissions from selected cities in North America, Europe, and East Asia observed by the TROPOspheric Monitoring Instrument (TROPOMI) before and after the COVID-19 pandemic. *Atmos. Chem. Phys.* **2023**, *23*, 8727−8748.
(59) Chunxia, J. 2024 tourism indicators in Xinjiang reached a historic high. *XinjiangDaily* **2025**. https://www.xinjiang.gov.cn/xinjiang/bmdt/202502/b3a471aa4f8843bd99bc5bed1eecf20d.shtml. (accessed 2026−10−21).
(60) National Bureau of Statistics of China. *National Bureau of Statistics of China*; 2025, https://www.stats.gov.cn/. (accessed 2025−08−14).
(61) *Organisation for Economic Co-operation and Development*; OECD Environmental Indicators, 2005. https://www.oecd.org/content/dam/oecd/en/publications/reports/2006/04/environment-at-a-glance_g1gh5bf1/9789264012196-en.pdf. (accessed 2026−10−21).
(62) Guo, Y.; Mao, X.; Wei, J.; Liu, M.; Chen, Y.; Zhou, J. Changes in the distance of interprovincial coal transportation in China and its effect on carbon emissions. *J. Transp. Geogr.* **2025**, *123*, 104139.

Downloaded from pubs.acs.org/esthag/article-pdf/doi/10.1021/acs.est.6c11406/6919082S/acs.est.6c11406.pdf by PEKING UNIV user on 19 November 2026

https://doi.org/10.1021/acs.est.6c11406
Environ. Sci. Technol. XXXX, XXX, XXX−XXX

(63) Xu, D.; Ma, Y.; Fan, Z.; Wang, B.; Zhang, H.; Wang, N.; Zhang, X.; Zhao, K. Evaluating air pollution and economic impacts in Chinese megacity clusters under clean air policies. *iScience* **2026**, *29* (7), 116492.
(64) Zhan, W.; Liao, Y.; Deng, J.; Wang, Z.; Yeh, S. Large-scale empirical study of electric vehicle usage patterns and charging infrastructure needs. *Npj Sustainable Mobility Transp.* **2025**, *2* (1), 9.
(65) Farzaneh, H.; Wang, X. Environmental and economic impact assessment of the Low Emission Development Strategies (LEDS) in Shanghai, China. *APN Sci. Bull.* **2020**, *10* (1), 26−33.
(66) Li, T.; Liu, Y.; Wang, C.; Olsson, G.; Wang, Z.; Wang, H. Decentralization of the non-capital functions of Beijing: Industrial relocation and its environmental effects. *J. Clean. Prod.* **2019**, *224*, 545−556.
(67) Shen, Y.; Shi, X.; Zhao, Z.; Sun, Y.; Shan, Y. Measuring the low-carbon energy transition in Chinese cities. *iScience* **2023**, *26* (1), 105803.
(68) Chen, J.; Wang, B.; Huang, S.; Song, M. The influence of increased population density in China on air pollution. *Sci. Total Environ.* **2020**, *735*, 139456.
(69) Wang, J.; Zhong, H.; Yang, Z.; Wang, M.; Kammen, D. M.; Liu, Z.; Ma, Z.; Xia, Q.; Kang, C. Exploring the trade-offs between electric heating policy and carbon mitigation in China. *Nat. Commun.* **2020**, *11* (1), 6054.
(70) Yuan, M.; Thellufsen, J. Z.; Lund, H.; Liang, Y. The first feasible step towards clean heating transition in urban agglomeration: A case study of Beijing-Tianjin-Hebei region. *Energy Convers. Manage.* **2020**, *223*, 113282.
(71) Chen, J.; Shan, M.; Xia, J.; Jiang, Y. Effects of space heating on the pollutant emission intensities in "2 + 26" cities. *Build. Environ.* **2020**, *175*, 106817.
(72) Cui, Y.; Zhang, W.; Wang, C.; Streets, D. G.; Xu, Y.; Du, M.; Lin, J. Spatiotemporal dynamics of CO2 emissions from central heating supply in the North China Plain over 2012−2016 due to natural gas usage. *Appl. Energy* **2019**, *241*, 245−256.
(73) Meng, W.; Zhu, L.; Liang, Z.; Xu, H.; Zhang, W.; Li, J.; Zhang, Y.; Luo, Z.; Shen, G.; Shen, H.; et al. Significant but Inequitable Cost-Effective Benefits of a Clean Heating Campaign in Northern China. *Environ. Sci. Technol.* **2023**, *57* (23), 8467−8475.
(74) Yang, X. F.; Liu, H.; Man, H. Y.; He, K. B. Characterization of road freight transportation and its impact on the national emission inventory in China. *Atmos. Chem. Phys.* **2015**, *15* (4), 2105−2118.
(75) Yu, C.; Dijkema, G. P. J.; de Jong, M.; Shi, H. From an eco-industrial park towards an eco-city: a case study in Suzhou, China. *J. Clean. Prod.* **2015**, *102*, 264−274.
(76) Cai, Z.; Hu, L.; Chen, D.; Zhang, Y.; Fang, X. Structural characteristics and drivers of greenhouse gas emissions at county-level and long-time scales: A case study of the Anji County, China. *J. Environ. Sci.* **2024**, *140*, 319−330.
(77) Zhang, H.; Shen, L.; Zhong, S.; Elshkaki, A. Coal resource and industrial structure nexus in energy-rich area: The case of the contiguous area of Shanxi and Shaanxi Provinces, and Inner Mongolia Autonomous Region of China. *Resour. Policy* **2020**, *66*, 101646.
(78) Xing, M.; Luo, F.; Fang, Y. Research on the sustainability promotion mechanisms of industries in China's resource-based cities—from an ecological perspective. *J. Clean. Prod.* **2021**, *315*, 128114.
(79) Yan, X.; Xu, Y.; Pan, G. Evolution of China's NOx emission control strategy during 2005 ~ 2020 over coal-fired power plants: A satellite-based assessment. *J. Environ. Manage.* **2023**, *348*, 119243.
(80) Zheng, X.; Lu, Y.; Yuan, J.; Baninla, Y.; Zhang, S.; Stenseth, N. C.; Hessen, D. O.; Tian, H.; Obersteiner, M.; Chen, D. Drivers of change in China's energy-related CO2 emissions. *Proc. Natl. Acad. Sci. U. S. A.* **2020**, *117* (1), 29−36.
(81) Zhao, P.; Zhang, M. The impact of urbanisation on energy consumption: A 30-year review in China. *Urban Climate* **2018**, *24*, 940−953.

Downloaded from pubs.acs.org/esthag/article-pdf/doi/10.1021/acs.est.6c11406/6919082S/acs.est.6c11406.pdf by PEKING UNIV user on 19 November 2026

https://doi.org/10.1021/acs.est.6c11406
Environ. Sci. Technol. XXXX, XXX, XXX−XXX